PHOTONICS Research

Tunable optical topological transition of Cherenkov radiation

TIANYU ZHANG,[1,2] XIAOQIUYAN ZHANG,[1,2] ZHUOCHENG ZHANG,[1,2] XINGXING XU,[1,2] YUEYING WANG,[1,2] ZHAOYUN DUAN,[1,2] YANYU WEI,[1,2] YUBIN GONG,[1,2] SHENGGANG LIU,[1,2] MIN HU,[1,2] AND TAO ZHAO[1,2,*]

[1]Terahertz Research Center, School of Electronic Science and Engineering, University of Electronic Science and Technology of China, Chengdu 610054, China
[2]Key Laboratory of Terahertz Technology, Ministry of Education, Chengdu 610054, China
*Corresponding author: forzhaotao@uestc.edu.cn

Received 29 April 2022; revised 18 May 2022; accepted 24 May 2022; posted 24 May 2022 (Doc. ID 462603); published 30 June 2022

Approaches to generate and manipulate Cherenkov radiation (CR) are challenging yet meaningful. Optical topological transition (OTT) in novel materials and metamaterials is also promising for modern photonics. We study the OTT of CR in graphene-based hyperbolic metamaterials (GHMs) for the first time. In GHMs, conventional and hyperbolic CR can be switched when crossing the topological transition frequency. This frequency can be altered by metamaterial components and external optical elements. For instance, external ultrafast optical pumps cause an ultrafast OTT from the elliptical to the hyperbolic state. Then, hyperbolic CR can be excited by low-energy electrons by leveraging the excellent photothermal properties of graphene. Hyperbolic CR vanishes when the GHM returns to its original state. Furthermore, graphene nonlocality occurs when the electron velocity is low enough, corresponding to a large wave vector. Concretely, when the electron velocity approaches the Fermi velocity of graphene, a nonlocality-induced OTT modifies the plasmonic properties of the GHM and brings a new lower velocity threshold of hyperbolic CR. Therefore, hyperbolic CR can only be induced in a limited velocity range. These findings pave the way for understanding CR properties in active plasmonic metamaterials and may be applied to complex photonic and polaritonic systems.

https://doi.org/10.1364/PRJ.462603

1. INTRODUCTION

Free-electron-based sciences, technologies, and installations have demonstrated enormous potential in fundamental physics, devices, and applications of photonics and optoelectronics [1–3]. The interactions between free electrons and materials or metamaterials can be used to generate radiation from the terahertz to the ultraviolet band [4,5]. The most widely known free-electron radiations include Cherenkov radiation (CR) [6–8], transition radiation [9,10], Smith–Purcell radiation [11], synchrotron radiation, and bremsstrahlung. Free-electron radiation depends not only on the parameters of free electrons but also on the complex local or nonlocal properties of the electromagnetic medium. Thus, we can control free-electron radiation by manipulating the environment (e.g., materials or structures) around electrons [12].

CR is one of the most widely studied categories of free-electron radiation. The earliest CR experiments were performed by Cherenkov and Vavilov in 1934 [13,14]. Then, their experimental results were theoretically explained by Tamm and Frank in 1937 [15]. CR is generated when the electron (or particle) velocity, u, exceeds the phase velocity of light in the medium, c/n, where c is the speed of light in free space (vacuum), and n is the (effective) refractive index of the medium. Since its discovery, CR has been used in various applications, including particle detectors and accelerators [16,17], high-power vacuum electronic sources and devices [18], and medical imaging [19].

Over the past two decades, the utilization of different natural materials and metamaterials has reignited research on CR [12]. For example, we found that surface plasmon polaritons supported by a noble metal film (e.g., Ag) excited by free electrons can be transformed into intense and coherent CR in the visible and ultraviolet bands [20]. However, a relatively high electron velocity (i.e., $u > c/n$) required for CR generation severely limits the feasibility of this method [21]. Other researchers then found that the strict electron velocity threshold for CR generation can be eliminated by a hyperbolic metamaterial (HMM) in the visible band, which can be composed of alternating nanometer-thin metal (e.g., Au) and dielectric (e.g., SiO_2) buffer layers [22]. Later, this concept was employed in silicon plasmonics by momentum-resolved electron energy loss spectroscopy in the ultraviolet band [23]. The latest results show that natural materials (e.g., hBN) can also be used to generate CR by low-energy electrons [24–26].

Besides, interesting CR phenomena can also be elicited in photonic crystals or designed metamaterials [27,28]. We have already demonstrated that reversed CR can be obtained experimentally from a left-handed material in the microwave band with opposite directions between the wave vector and energy flux [29]. In addition to CR properties, we also devised a new mechanism of direction-controllable inverse transition radiation in a graphene multilayer structure working in the terahertz and mid-infrared bands [30]. Compared with the general case, transition radiation generated in this structure is dramatically enhanced. Recently, we also found that in-plane CR can be generated efficiently in the graphene hyperbolic grating, achieving a stronger CR than that generated in normal graphene-based HMMs (GHMs) [31].

Considering different topological materials and structures, topological photonics is being rapidly developed and can be applied to control the properties of light in different media [32,33]. For example, the optical topological transition (OTT) in some metamaterials enables innovative and effective control [32–34]. The OTT can also appear in HMMs and natural hyperbolic materials [34–36]. If the OTT occurs in an HMM, its topological iso-frequency surface can transform from ellipsoid to hyperboloid and vice versa. This phenomenon can be applied to manipulate light–matter interactions in HMMs, such as the spontaneous emission rate of nearby emitters [34]. With the development of theoretical and experimental techniques in recent years, the OTT can also be induced in natural materials by external ultrafast optical pump beams [36]. Thus, the topology phase of the iso-frequency surface of GHMs can be switched between ellipsoid and hyperboloid in an ultrafast manner.

In this study, we determined the importance of the OTT to generate and manipulate CR in GHMs, in which the OTT frequency, f_t, directly correlates to the generating conditions of CR, such as the required electron velocities and frequency range. When the working frequency crosses f_t, the GHM switches from the elliptical state to the hyperbolic state or vice versa. In the elliptical state, only conventional CR can be excited by high-energy electrons. However, in the hyperbolic state, hyperbolic CR can be induced even by low-energy electrons. We also devised methods to analyze the OTT of CR in the GHM, including macroscopic effective medium theory (EMT) and microscopic scattering-matrix theory (SMT). Based on our theoretical derivations and numerical calculations, the OTT of CR in the GHM is comprehensively characterized and analyzed. Specifically, we emphasize two novel OTT-induced phenomena involving the photothermal property and nonlocality of graphene. We indicate that not only the plasmonic dispersion is modified, but additional CR phenomena are induced in the GHM. The photothermal property can be used as novel ultrafast CR sources, and nonlocality enables a new lower velocity threshold of CR. Finally, we summarize results, draw conclusions, and present future research directions.

2. METHOD

In this section, we present the methods to analyze the GHM properties and then calculate and explain several phenomena related to the OTT of CR in the GHM. First, the basic structure of the studied GHM for this work is described. Then, the macroscopic EMT and microscopic SMT are detailed. Finally, three widely used graphene conductivity models are presented, including the classical Drude model, photothermal (temperature-dependent) model, and nonlocal model (wave-vector-dependent), which is based on random-phase approximation with relaxation-time approximation. Note that, among these three models, only the last model considers momentum- or wave-vector-dependent effects, but just the function of frequency.

A. GHM

We use a graphene-dielectric multilayer structure as the platform of the HMM for CR because graphene provides numerous advantages as the metallic part of the HMM [37]. Remarkably, graphene possesses excellent tunable electrical/optical properties, broadband and ultrafast optical response (especially in the terahertz and mid-infrared bands), high electron mobility and low energy consumption [38], and wave-vector-dependent or nonlocal property [39]. As a result, GHMs can establish a promising platform for tunable CR-based sources, detectors, and devices.

The proposed GHM for CR is illustrated in Fig. 1. Free electrons with constant velocity u move parallel to the positive x axis at a constant distance on top of the GHM. The GHM is composed of alternating graphene and dielectric buffer layers. In this work, just for convenience, we keep the number of graphene layers unchanged (equal to 10) because the conclusions for CR in the GHM would not change in the case of different graphene layers. Owing to the field polarization induced by moving electrons, without loss of generality, we only consider the transverse magnetic polarization and neglect the effect on the y axis (Fig. 1).

B. Macroscopic EMT

The thicknesses of the graphene and dielectric buffer layers in our GHM are much lower than the considered wavelengths. Therefore, the GHM can be approximated as a homogeneous

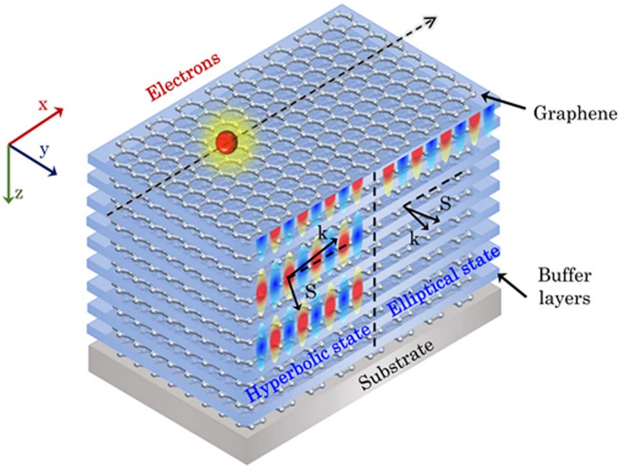

Fig. 1. CR excited by low-energy electrons in the GHM. Features of the hyperbolic CR in the hyperbolic state (left half) and conventional CR in the elliptical state (right half).

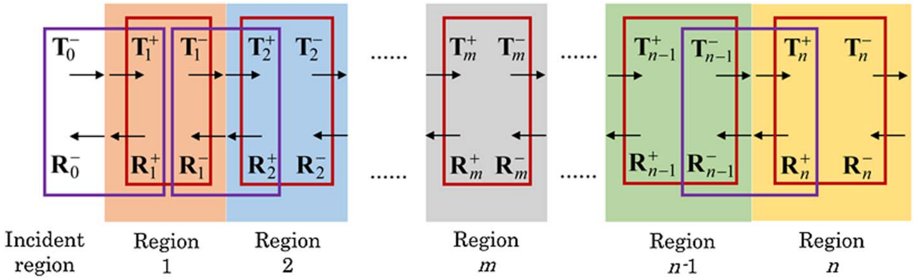

Fig. 2. Basic principles of SMT. T and R represent the transmission and reflection coefficients, respectively. The purple and red boxes indicate the connection of scattering matrices in the interface and inside the region, respectively.

anisotropic medium described by the macroscopic EMT [40], which provides its effective in-plane (parallel) and out-of-plane (perpendicular) permittivity components.

The effective permittivity component of the GHM can be approximated using previous results [41,42]. By the EMT, we can analyze the OTT of CR generated in the GHM, including the effective in-plane and out-of-plane permittivity components, $\varepsilon_{\text{eff-in}}$ and $\varepsilon_{\text{eff-out}}$, respectively, the effective refractive index, n_{eff}, the propagating directions of wave vector θ_k and energy flux θ_S, and the effective power density spectrum of CR. In Sections 3, these parameters and some related formulas of EMT are presented in detail.

C. Microscopic SMT

From the microscopic perspective, the dispersion relation and field distribution of plasmon modes inside the GHM can be calculated by rigorously applying the SMT. According to the SMT, multiple plasmon modes inside the GHM can be excited flexibly by altering the electron velocities. Interactions between these plasmon modes are complicated and make them deviate from their original positions. Effective hyperbolic CR generated in the GHM is the superposition of coupled plasmon modes, especially acoustic modes.

By adapting the existing SMT [43,44], we calculate the imaginary part of the reflection coefficient, $\text{Im}(r_p)$, of the GHM, which indicates the dispersion of the supported modes in an optical system, such as plasmonic and phononic modes. We also consider boundary matching conditions in the presence of 2D surface current density (using graphene conductivity). The basic principles of this method are described as follows and illustrated in Fig. 2.

In the SMT, each interface and region is represented by a 2×2 optical matrix called a scattering matrix (S-matrix). If there are n interfaces, then $2n$ S-matrices are defined. By simple equivalent mathematical operations, H- and G-matrices can be derived by S-matrices. Then, I-matrices are calculated through H- and G-matrices, which describe the transmission and reflection properties of each interface. Finally, the field distribution of plasmon modes with given frequencies and wave vectors can be recovered through I-matrices. Notably, the clinodiagonal elements of the propagating matrix in the SMT are consistent, substantially differing from the transfer matrix method. As a result, the SMT provides higher numerical stability than the transfer matrix method. Similar processes of the SMT can also be found in very recent studies that have also considered the nonlocality of noble metals [43,44].

D. Conductivity Model of Graphene

The most used conductivity model of graphene is the classical Drude model, which only considers intraband electron transition and often neglects temperature-dependent effects in highly doped graphene [37,39]. However, the chemical potential of graphene depends on the temperature of graphene electrons when it is high enough. With highly efficient and ultrafast thermodynamic properties, electrons can be heated instantaneously when an ultrafast laser illuminates graphene, while the temperature of crystal lattice remains almost unchanged. Therefore, the photothermal properties of graphene optical conductivity should be described by a modified model involving electron temperature [35,45]. In this work, we suggest that graphene photothermal conductivity can be used to analyze the ultrafast OTT of CR in the GHM. It can be caused under the illumination of an external optical pump, as explained in Section 3.

On the other hand, when the electron velocity is low enough, it causes a large wave vector. When this happens, graphene nonlocality should be considered. Based on the widely used nonlocal random-phase approximation graphene nonlocal conductivity model, which neglects the interaction between graphene electrons, we investigate the effects of graphene nonlocality on the OTT of CR in the GHM. In addition to dispersive modifications, it also brings a new lower velocity threshold to achieve the OTT for CR. This velocity threshold is roughly equal to the Fermi velocity of graphene, at which electrons enter the electron-hole continuum or Landau damping region [39]. Strictly, the nonlocal phenomena of quantum materials should be analyzed by further theoretical methods, such as quantum-corrected hydrodynamics and microscopic surface-response functions, which are beyond the scope of this work.

3. RESULTS AND DISCUSSION

In this section, we first use the classical Drude model for analysis. Then, the photothermal and nonlocal models are used to analyze the electron temperature- and wave-vector-dependent effects of CR in the GHM.

The EMT allows for describing the effective permittivity components of the GHM accurately. Specifically, the effective permittivity of graphene, ε_g, can be described as [41,42]

$$\varepsilon_g(\omega) = 1 + \frac{i\sigma_g(\omega)}{\varepsilon_0 \omega t_g}. \tag{1}$$

In addition, the effective in-plane and out-of-plane permittivities of the GHM can be well described as [41,42]

$$\varepsilon_{\text{eff-in}} = f\varepsilon_g + (1 - f)\varepsilon_b, \varepsilon_{\text{eff-out}} = \frac{1}{f/\varepsilon_g + (1 - f)/\varepsilon_b}, \tag{2}$$

respectively, where $f = t_g/(t_g + d)$ is the filling factor of graphene, t_g and d are the thicknesses of graphene and the dielectric buffer, respectively, and ε_b is the permittivity of the dielectric buffer.

The effective reflective index n_{eff} of the GHM can be described as [22]

$$n_{\text{eff}}(\omega, u) = \sqrt{\varepsilon_{\text{eff-in}} + \left(1 - \frac{\varepsilon_{\text{eff-in}}}{\varepsilon_{\text{eff-out}}}\right)\left(\frac{c}{u}\right)^2}, \tag{3}$$

which depends on not only frequency but the velocities of free electrons.

According to the EMT, the real part of the effective in-plane permittivity, $\text{Re}(\varepsilon_{\text{eff-in}})$, is shown in Figs. 3(a) and 3(b). $\text{Re}(\varepsilon_{\text{eff-in}})$ is negative at low frequencies and becomes positive at high frequencies. At the OTT frequency f_t, $\text{Re}(\varepsilon_{\text{eff-in}})$ equals zero. When we change d, and the Fermi level of graphene E_F, f_t shifts accordingly. For example, for E_F of 0.15 eV, if we decrease d from 300 to 30 nm, f_t increases from 8.6 to 27.1 THz [Fig. 3(a)]. For d of 30 nm, if we increase E_F from 0.15 to 0.35 eV, f_t increases from 27.1 to 41.5 THz [Fig. 3(b)]. Hence, we can select f_t by simply altering related dielectric and graphene parameters. When $\text{Re}(\varepsilon_{\text{eff-in}})$ is negative (positive), the GHM exhibits the hyperbolic (elliptical) properties, which decide whether CR can be induced by low-energy electrons.

With the effective in-plane permittivity components [Figs. 3(a) and 3(b)], we can obtain n_{eff} and normalized electron velocity, $v_n = u \cdot n_{\text{eff}}/c$, for CR in the GHM at different electron velocities, as shown in Figs. 3(c) and 3(d).

If the electron velocity is lower or higher than the phase velocity of light in the dielectric buffer layer, $v_b = c/n_b = 2c/3$, where $n_b = 1.5$ is the refractive index of the dielectric buffer, the dependence of n_{eff} on the frequency considerably varies. When $u > v_b$ $(u < v_b)$, n_{eff} increases (decreases) with increasing frequency and is smaller (larger) than c/v_b below f_t [Fig. 3(c)]. Figure 3(d) shows that the highest frequency for CR generation by low-energy electrons is f_t. In other words, the hyperbolic state of the GHM induces a large n_{eff} and allows CR generation by low-energy electrons $(u < v_b)$ below f_t. On the other hand, the elliptical state of the GHM excited by high-energy electrons $(u > v_b)$ corresponds to conventional CR generation.

Shortly, in the GHM, n_{eff} changes greatly, especially in the hyperbolic region [Fig. 3(c)]. Furthermore, with n_{eff}, we can calculate v_n [Fig. 3(d)], which can help us to decide whether CR can be generated at a working point (frequency

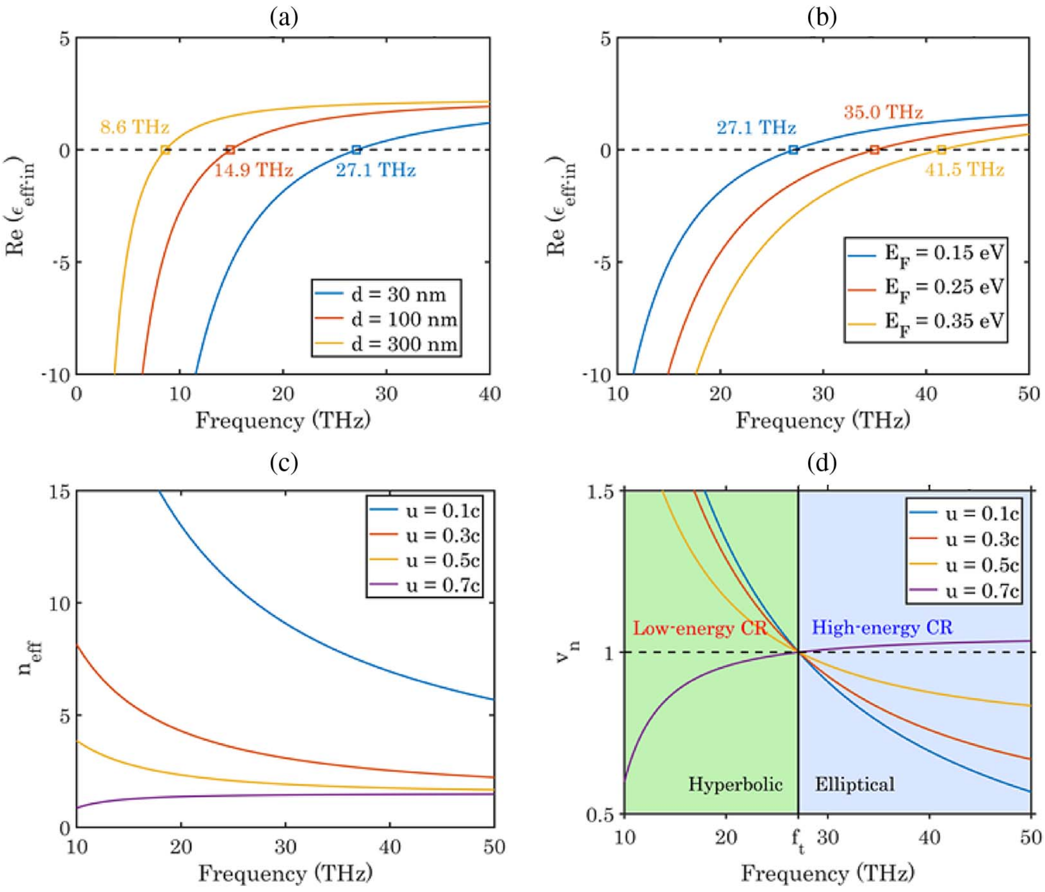

Fig. 3. Effective in-plane permittivity of the GHM described by the EMT. $\text{Re}(\varepsilon_{\text{eff-in}})$ for (a) $E_F = 0.15$ eV and (b) $d = 30$ nm. (c) Effective refractive index n_{eff} and (d) normalized electron velocity v_n at different electron velocities, $E_F = 0.15$ eV, and $d = 30$ nm (f_t, OTT frequency).

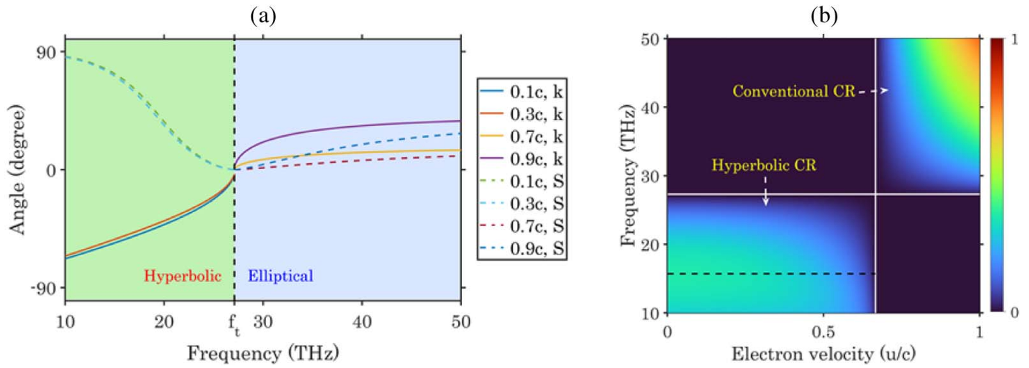

Fig. 4. Effective CR properties. (a) Directions of wave vector k and energy flux S. (b) Normalized CR intensity (for $E_F = 0.15$ eV and $d = 30$ nm).

and electron velocity). If $v_n > 1$, then CR can be generated. When the GHMs locate in a hyperbolic state, this condition can only be satisfied by low-energy electrons. When we decide whether CR can be induced, we need to consider the dispersion of the whole optical system. Specifically, in this work, the modes that can be supported in the GHM (hyperbolic state) require extremely high wave vectors, which can only be provided by low-energy electrons (e.g., $u = \omega/q$). Therefore, CR can only be generated by low-energy electrons when the GHM locates in the hyperbolic state.

We can also obtain the directions for effective CR, including wave vector k and energy flux S. The corresponding results are shown in Fig. 4(a). When $u < v_b$ (e.g., $u = 0.1c$, $0.3c$), the directions of k and S (relative to the x axis) differ. Although they still propagate forward, there exists an angle between them, which can be as large as 180° (antiparallel) below f_t. However, when $u > v_b$ (e.g., $u = 0.7c$, $0.9c$), the directions of k and S are nearly the same, with a small discrepancy caused by the anisotropic permittivity components along with the parallel and perpendicular directions of the GHM. In addition, Fig. 4(a) shows that different electron velocities have distinct effects on the CR angles. When $u > v_b$, the CR angles increase with higher electron velocities. When $u < v_b$, they remain nearly unchanged with different electron velocities, being consistent with the property of an HMM in the limit of large wave vectors.

The normalized effective CR spectrum is shown in Fig. 4(b). There exist two regions for CR. For high-energy electrons ($u > v_b$), only conventional CR can be induced above f_t [top right region of Fig. 4(b)]. Below f_t, the GHM expresses hyperbolic properties, and v_n is lower than the unit, impeding CR generation. On the other hand, for low-energy electrons ($u < v_b$), hyperbolic CR occurs below f_t [bottom left region of Fig. 4(b)]. Both higher working frequencies and electron velocities can improve the intensity of conventional CR. In contrast, the strongest hyperbolic CR occurs at relatively low frequencies around 15 THz [black dashed line in the bottom left region of Fig. 4(b)], and slower electrons can even slightly increase the CR intensity. More interestingly, although the electron velocity is much lower, the strength of hyperbolic CR can be comparable to that of conventional CR because their intensities are in the same order of magnitude.

The EMT allowed us to demonstrate that the GHM, which serves as a tunable HMM, can be used in principle as an ideal platform for CR generation using low-energy electrons. The main parameter that determines the generation of CR inside the GHM is the OTT frequency f_t, which sets the frequency range for CR. According to our results, CR can be generated by extremely low electron velocities at frequencies below f_t, which is tunable by graphene and dielectric parameters in the GHM. Nevertheless, the EMT treats the whole GHM as a system and uses effective permittivity components to calculate the properties of CR in the GHM. To unveil the detailed behaviors inside the GHM and discuss the generation of hyperbolic CR even by low-energy electrons, we should use a microscopic method for analysis.

To determine the specific behavior inside the GHM, we should calculate the supported plasmonic modes and dispersion properties of the GHM by an optical matrix method such as the SMT [43,44]. The SMT provides the imaginary part of the reflection coefficient, $\mathrm{Im}(r_p)$, of the GHM to obtain the dispersion of plasmon modes shown in Figs. 5(a) and 5(b). The 2D plane of plasmon dispersion can be approximately divided into two areas separated by f_t [27.1 THz, white dashed line in Fig. 5(a)]. Above f_t, only one plasmon mode (i.e., optical mode) can be excited, indicating that plasmonic interaction between the graphene layers is relatively weak. Below f_t, multiple plasmon modes are supported, indicating strong coupling between different graphene plasmon modes. Although all plasmon modes have higher frequencies when they are excited by slower electrons, the intensity of a plasmon mode in the hyperbolic region is much smaller than that in the elliptical region because the plasmonic interactions redistribute the weight among different plasmon modes.

If the plasmon modes have larger wave vectors, they are weaker and more difficult to be excited. For example, except for the strongest optical plasmon mode [the rightmost one in Fig. 5(a)], other plasmon modes are weaker. The most intense position of $\mathrm{Im}(r_p)$ in the hyperbolic region appears at a finite frequency point roughly at 15 THz, being consistent with the effective CR spectrum shown in Fig. 4(b). Hence, effective CR is closely related to the plasmon modes supported in the GHM. Furthermore, at almost any electron velocity satisfying $u < v_b$ (e.g., $0.01c$–$0.05c$), several plasmon modes can be

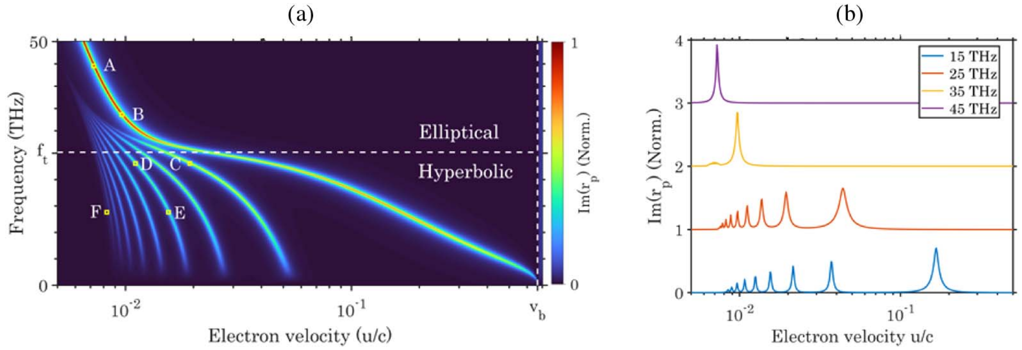

Fig. 5. (a) Dispersion of plasmon modes in the GHM characterized by the imaginary part of reflection coefficient, $\mathrm{Im}(r_p)$, displayed in $\log_{100}$ scale. (b) Imaginary part of reflection coefficient: $\mathrm{Im}(r_p)$ at 15, 25, 35, and 45 THz.

excited simultaneously. These modes contribute to the hyperbolic properties of the GHM and occur in the broad frequency range below f_t. When $u > v_b$, the GHM expresses elliptical properties, and it is unable to support any plasmon mode, thus impeding hyperbolic CR generation.

Suitable GHM topological states and electron velocity should be simultaneously provided to ensure CR generation. If the system locates in the hyperbolic state, the plasmon modes can be excited by low-energy electrons, and effective hyperbolic CR can be generated. In contrast, if it exhibits elliptical properties, the plasmon modes cannot be excited, and CR can only be induced by high-energy electrons. From the plasmon dispersion, we can analyze the OTT of CR in the GHM from the hyperbolic state to the elliptical state. In Fig. 5(b), we select some frequencies below and above f_t, and observe plasmon mode excitation. Below f_t (e.g., 15, 25 THz), the optical and acoustic plasmon modes can be excited simultaneously. With increasing frequency, the excitation of all plasmon modes requires lower electron velocities. Above f_t (e.g., 35, 45 THz), the acoustic plasmon modes cannot be observed now, and only the optical plasmon mode can be excited. In other words, in the GHM, the existence of hyperbolic CR depends on whether the acoustic plasmon modes can be excited.

The field distribution of graphene plasmon modes indicates that effective CR generation is essentially the superposition of coupled propagating plasmon modes excited in each graphene layer, which notably differs from the mechanism of conventional CR generated in normal media. By the SMT, the representative spatial field distribution of plasmon modes in the GHM is shown in Fig. 6 and corresponds to the points labeled by white letters in Fig. 5(a), in which we also indicate the directions of effective CR calculated by the EMT [Figs. 6(c)–6(f)]. The white dashed lines in Fig. 6 indicate the positions of graphene layers.

For frequencies above f_t, only the optical plasmon modes can be excited in the topmost graphene layer, but this excitation can hardly spread to the bottom graphene layers owing to insufficient coupling and high loss. Compared with the plasmon mode excited at point B, the mode at point A has a much higher wave vector, which leads to stronger field confinement in the direction parallel to the z axis [Figs. 6(a) and 6(b)]. In these cases, CR cannot be generated in the GHM by low-energy electrons.

For frequencies below f_t, the plasmon modes can propagate inside the GHM, as shown in Figs. 6(c)–6(f). The distributions for the second and fourth modes at 25 THz and the fourth mode at 15 THz are shown in Figs. 6(c)–6(e). For modes with higher wave vector and higher frequency, the required electron velocity to excite plasmon mode is lower, indicating that they have larger wave vectors and higher confinements. In Fig. 6(f), given the propagation loss of graphene, the plasmon intensity

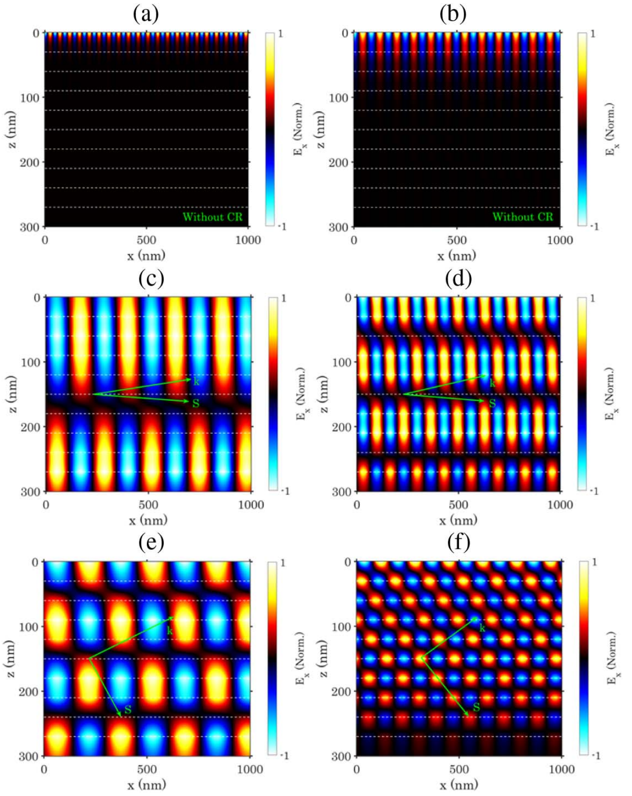

Fig. 6. Electric field spatial distributions of excited plasmon modes parallel to the x axis corresponding to the white labels shown in Fig. 5(a). (a) Point A with the optical mode at 45 THz. (b) Point B with the optical mode at 35 THz. (c) Point C with the second mode at 25 THz. (d) Point D with the fourth mode at 25 THz. (e) Point E with the fourth mode at 15 THz. (f) Point F with the tenth mode at 15 THz. The white dashed lines indicate graphene layers.

in the very bottom graphene layer is much weaker than that in the topmost layer. This represents the 10th mode at 15 THz, which is hard to observe in Fig. 5(a). However, it still enables CR generation, as described approximately by the EMT results shown in Fig. 4. The effective hyperbolic CR in the GHM is composed of evanescent waves (graphene plasmon polaritons) instead of propagating waves. The coupling between different plasmon modes establishes an effective propagating field. Similar phenomena can also be found in our previous study on transition radiation [30].

Although the properties of hyperbolic CR can be altered by various parameters of the GHM, active optical manipulating methods of CR remain to be devised. Instead of electrical tuning of the Fermi level of graphene, we propose the concept of an ultrafast CR source by leveraging the photothermal effect of graphene [35,45]. The temperature-dependent effects of graphene electrons can be used to induce ultrafast OTT in the GHM given the extremely small electronic heat capacity of graphene. On the other hand, conventional electrical tuning is difficult to implement in a multilayer structure, rendering optical modulation of graphene properties more attractive.

Hot carriers in graphene are generated almost instantaneously in an ultrafast response caused by an external ultrafast optical pump [35,45]. Ultrafast photothermal properties can be obtained owing to advantages of graphene such as low carrier density and high carrier mobility, low electronic heat capacity, large variation of the optical response induced by electronic heating, and relatively weak electron-phonon interactions, all of which result in the ultrafast and substantial photothermal response of graphene. With an optical pump, graphene undergoes ultrafast heating (<1 ps) and much slower cooling (in the order of a few picoseconds) processes. Besides, graphene electrons can reach extremely high temperatures, notably exceeding the crystal lattice temperature. As a result, the temperature of graphene electrons can achieve several thousands of kelvins in extremely short time scales [35,45].

In our calculations, we only use the possible temperature range of graphene electrons to calculate temperature-dependent conductivity. Strictly, in this case, the ultrafast pump-induced effects of graphene should be considered in the analysis. However, we notice that some works already get several beautiful results of that, by which the temperature and graphene conductivity can be calculated in a consistent manner [35,45]. On the other hand, in this work, we only hope to theoretically reveal the possibility of this ultrafast pump-induced OTT of CR in the GHMs. The calculation and analysis of the entire ultrafast pump-induced processes in graphene are beyond the scope of this work.

The graphene conductivity considering photothermal effects can be calculated as [35,45]

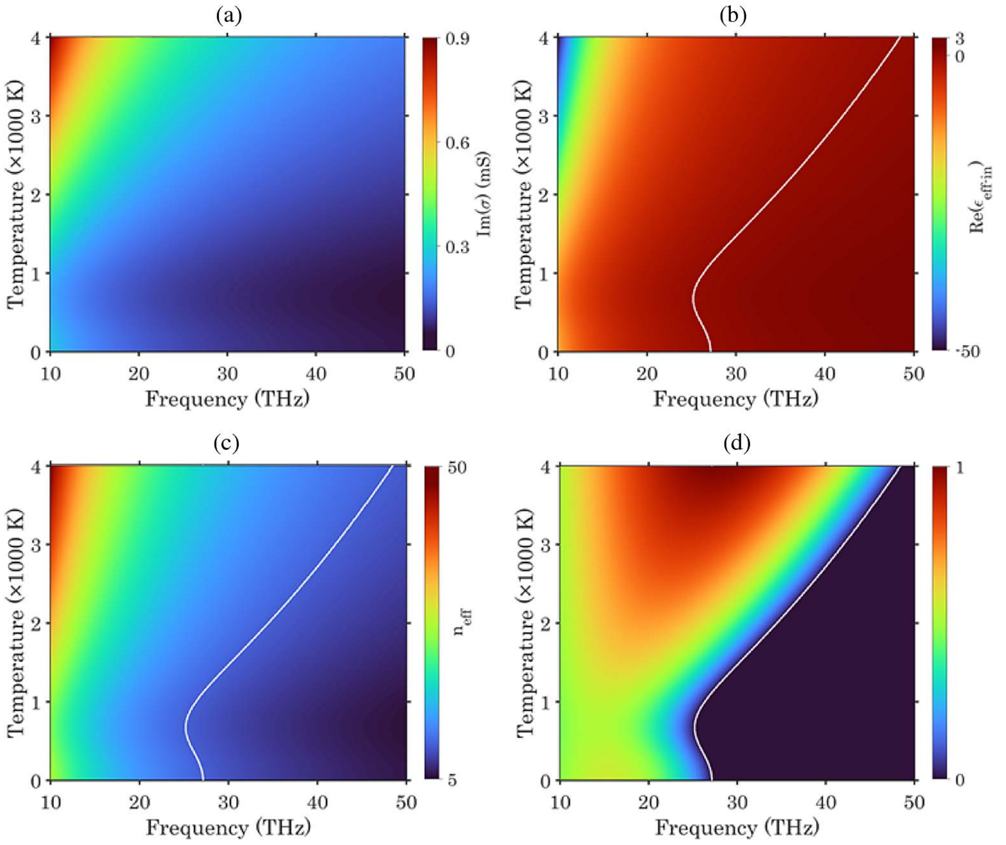

Fig. 7. Temperature-dependent photothermal properties. (a) Imaginary part of temperature-dependent conductivity, $\mathrm{Im}(\sigma)$. (b) Real part of temperature-dependent effective in-plane permittivity, $\mathrm{Re}(\varepsilon_{\text{eff-in}})$. The white line indicates $\mathrm{Re}(\varepsilon_{\text{eff-in}}) = 0$. (c) Effective refractive index n_{eff} at $u = 0.1c$. The white line indicates $n_{\text{eff}} = 10$, or $v_n = 1$. (d) Normalized CR intensity at $u = 0.1c$. The white line indicates the boundary for CR generation.

$$\sigma(\omega) = \frac{e^2}{\pi\hbar^2}\frac{i}{\omega + i\tau^{-1}} \times \left\{\mu^D - \int_0^\infty \mathrm{d}E \frac{f(E) - f(-E)}{1 - 4E^2/[\hbar^2(\omega + i\tau^{-1})^2]}\right\}, \quad (4)$$

in which the chemical potential of graphene depending on electronic temperature T_e can be described by

$$\mu^D = \mu + 2k_B T_e \ln\{1 + \exp[-\mu/(k_B T_e)]\}, \quad (5)$$

$$\mu = \sqrt{\sqrt{E_F^4 + (2\log^2 4)^2 (k_B T_e)^4} - 2(2\log^2 4)(k_B T_e)^2}. \quad (6)$$

According to these formulas, the imaginary part of the temperature-dependent graphene conductivity, $\mathrm{Im}(\sigma)$, is shown in Fig. 7(a). $\mathrm{Im}(\sigma)$ is strongly dependent on the electronic temperature of graphene instead of the background (e.g., crystal lattice) temperature, and it will increase if the frequency decreases and/or the temperature increases. Then, $\mathrm{Re}(\varepsilon_{\text{eff-in}})$ can be directly obtained from the relation between permittivity and conductivity [Eqs. (1) and (2)], as shown in Fig. 7(b). The entire process of ultrafast heating and cooling is conducive to the ultrafast OTT that allows the GHM to switch from the elliptical state at low temperatures to the hyperbolic state at high temperatures and eventually return to the original elliptical state. This process takes approximately several picoseconds entirely.

Concretely, for example, consider a CR frequency of 30 THz. When $\mathrm{Re}(\varepsilon_{\text{eff-in}})$ is positive at a low temperature (e.g., <1000 K), CR cannot be generated with low-energy free electrons. However, $\mathrm{Re}(\varepsilon_{\text{eff-in}})$ becomes negative when the temperature increases above 2000 K. CR can be generated by low-energy electrons now because the GHM expresses hyperbolic properties. $\mathrm{Re}(\varepsilon_{\text{eff-in}})$ becomes positive again when the temperature reduces below the critical temperature, and hyperbolic CR fades. In other words, n_{eff} increases with the electron temperature at most frequencies [Fig. 7(c)], and once the condition for CR generation is satisfied (i.e., $v_n > 1$), hyperbolic CR can be excited. With this behavior, we can calculate the effective CR spectrum at different temperatures, as shown in Fig. 7(d). Effective CR is induced at high temperatures in a broad frequency range corresponding to regions where $\mathrm{Re}(\varepsilon_{\text{eff-in}})$ is negative. We propose that this novel principle can be applied to develop ultrafast integrated CR sources, detectors, and other devices in the future.

We have demonstrated that the macroscopic EMT and microscopic SMT could unveil basic properties of effective CR and plasmon modes excited by low-energy electrons in the GHM, in which the electron velocity for excitation can be $0.01c$ or even lower. However, at such low electron velocities, the wave vector carried by free electrons can be extremely large. Hence, the nonlocal (wave-vector-dependent) properties of graphene should be considered because it affects CR generation.

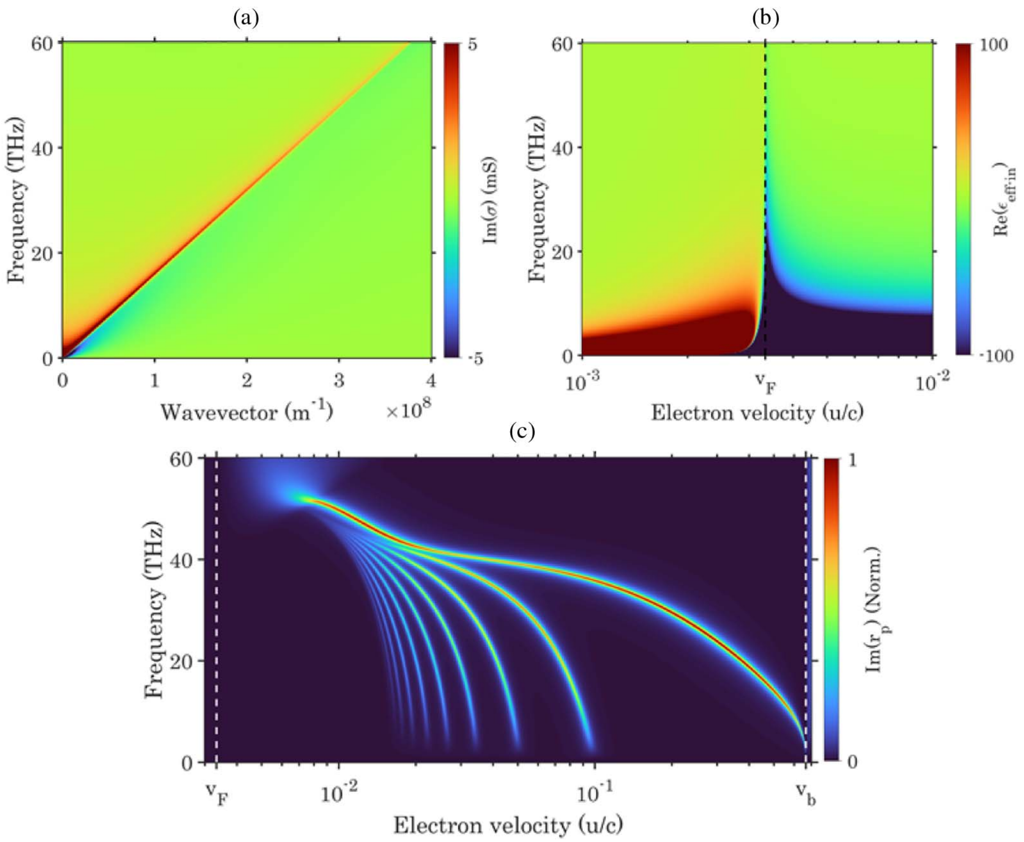

Fig. 8. Nonlocal properties. (a) Imaginary part of nonlocal graphene conductivity, $\mathrm{Im}(\sigma)$. (b) Real part of effective in-plane permittivity, $\mathrm{Re}(\varepsilon_{\text{eff-in}})$. The black dashed line indicates the new lower electron velocity threshold for CR, which is equal to the Fermi velocity of graphene, v_F. (c) Dispersion relation: the imaginary part of the reflection coefficient, $\mathrm{Im}(r_p)$, is displayed on $\log_{100}$ scale. The white dashed lines indicate the positions of the Fermi velocity of graphene, v_F, and the phase velocity of light in the buffer layer, v_b.

Nonlocal properties of CR have recently been studied in multilayer metal-dielectric structures, with the nonlocal properties of the metal being caused by finite structural dimensions and the nonlocal nature of metallic electrons [43,44,46]. Given the extremely strong many-body effects in graphene, including complex electron-electron and electron-phonon interactions, nonlocality is considerable in many cases [47].

For demonstration, we use the widely used nonlocal graphene conductivity model based on random-phase approximation with relaxation-time approximation, which disregards the many-body interactions between electrons [47]. The imaginary part of the nonlocal graphene conductivity, $\mathrm{Im}(\sigma)$, is shown in Fig. 8(a). The properties of $\mathrm{Im}(\sigma)$ substantially differ from those in the low-wave-vector limit. When the wave vector approaches the Fermi wave vector of graphene, k_F, $\mathrm{Im}(\sigma)$ initially increases to large positive values and then suddenly becomes negative when the wave vector is higher than k_F. This unusual property occurs when the quasiparticles decay into electron-hole pairs. The corresponding region is usually determined by the electron-hole continuum or Landau damping region [47].

Then, the real part of the nonlocal effective in-plane permittivity, $\mathrm{Re}(\varepsilon_{\text{eff-in}})$, is shown in Fig. 8(b). A lower bound of the electron velocity for CR generation appears near the Fermi velocity of graphene, $v_F \approx 10^6\ \mathrm{m/s} = c/300$. This new lower threshold of CR in the GHM is induced due to the OTT appearing when the wave vector carried by electrons is larger than k_F. Therefore, hyperbolic CR can only be induced at electron velocities between v_F and v_b. The dispersion curve of plasmon modes considering the nonlocality of graphene is shown in Fig. 8(c). Compared with the local result shown in Fig. 5(a), a lower bound of velocity appears, and the dispersion curve with nonlocality shows differences, such as the blueshift of the plasmon frequency. Specifically, at a given electron velocity, the frequency of the plasmon mode considering nonlocality is much higher than that in the local case. This effect has also been reported in the plasmonic properties of metal described by the hydrodynamic model [48].

4. CONCLUSION AND OUTLOOK

In this work, we comprehensively studied the OTT of CR in the GHMs theoretically for the first time. We propose that the topological phase or the OTT frequency of the GHM determines the feasibility of CR generation by low-energy electrons. These parameters can be modified by various factors in regions such as the graphene and dielectric parameters. They can also be manipulated by an external optical pump in an ultrafast manner. In the GHMs, hyperbolic CR, also known as threshold-free CR, is produced by the superposition of plasmon modes excited in different graphene layers effectively. Both the topological state and electron velocity should be adjusted to ensure CR generation. Combining the advantages of the EMT and SMT, we can clarify the detailed mechanisms of the OTT of CR in the GHMs from both macroscopic and microscopic perspectives. Moreover, the nonlocality and ultrafast pump-induced photothermal properties of CR in hyperbolic media are also important and should be considered in future work.

Nevertheless, our results are achieved without considering the effects of the many-body interactions in graphene, and the GHM is only one of the hyperbolic media, both of which should be extended to satisfy more complex and broader situations in the future. Specifically, the Fermi velocity of graphene is treated as a constant value throughout this work. However, the Fermi velocity of graphene is just the nonlocality-induced lower velocity threshold of CR in the GHMs. As far as we know, the Fermi velocity of graphene can be tuned by the electron-electron interactions [49]. By this method, the Fermi velocity of graphene can be promoted near threefold (3×10^6 m/s), compared to the normal value (1×10^6 m/s). Furthermore, we notice that the substrate [50], carrier-carrier screening effect [51,52], twisted bilayer graphene structure [53], electron-phonon interactions [54], and vacuum fluctuations [55] can be applied to tune the Fermi velocity of graphene, which is necessary for the tuning of the lower velocity threshold of hyperbolic CR.

For the experimental demonstration in the future, it requires two main technical conditions as follows: first, the effective fabrication and electrical tuning of high-quality graphene and the GHMs; second, the efficient production and flexible controlling of the free electrons, and the precise electromagnetic radiation measurements. For the former, previous experimental results indicate that the fabrication and manipulation of the GHMs in the mid-infrared are achievable and realizable [41,42]. For the latter, previous experimental results indicate the feasibility of the observation of the interactions between HMMs and free electrons [17,22]. Additionally, in this work, we also propose an ultrafast CR device caused by the ultrafast photothermal effects of graphene. In recent research, experimental achievements in the fields of ultrafast lasers and ultrafast electron pulses can provide high-performance measurements [1–5]. With the developments in ultrafast lasers and ultrafast electron pulses, we believe our designs can be realized in the future.

Although the OTT of CR in the GHMs is well investigated in this work, the properties and applications of OTT can hardly cover. Specifically, the OTT can make wave propagation in the forbidden directions of the optical systems [56], produce the optical spin–Hall effect [57], and so on. For the optical devices based on OTT, these include the hyper-lens [58], the epsilon-near-zero devices [59], and the solar cell for energy transfer [60]. With the development of topological photonics, the effects and devices based on the OTT can be achieved in the future [32–34].

On the other hand, in the terahertz and mid-infrared bands, many optical phenomena associated with the OTT can be achieved in materials and metamaterials, and these materials and metamaterials can be controlled by electronic, magnetic, and thermionic methods [61–63]. We believed that these materials and metamaterials that possess brilliant properties can be combined with free electrons in the future and can provide more possibilities in the research of the terahertz and mid-infrared sources, devices, and applications.

The interaction between free electrons and materials or metamaterials is expected to gain importance in future research and applications. In addition to graphene, various natural materials can be used as platforms for studying free-electron-based light–matter interactions, such as hexagonal boron nitride, transition metal dichalcogenides, topological materials, and other polariton materials [64]. The ultrafast property of electrons will be another hotspot for studying and using light–matter interactions based on intense ultrafast laser and free-electron sources [1–3]. Efficient, compact, low-cost, and highly tunable stimulated-CR and CR-based free-electron laser sources, detectors, and electronic/photonic devices are challenging to develop yet promising.

We expect that the mechanisms, explanations, and findings of this study will support future work in the field. Free-electron-based sciences, technologies, and applications will continue expanding, and we believe that our work is valuable for understanding complex interactions between free electrons and novel materials/metamaterials. Furthermore, our findings may pave the way for the development of future high-performance integrated and tunable free-electron-based light sources, devices, and applications.

Funding. National Key Research and Development Program of China (2017YFA0701000, 2020YFA0714001); National Natural Science Foundation of China (61921002, 61988102, 62071108, 62131006); Fundamental Research Funds for the Central Universities (ZYGX2020ZB007).

Disclosures. The authors declare no conflicts of interest.

Data Availability. Data underlying the results presented in this paper are not publicly available at this time but may be obtained from the authors upon reasonable request.

REFERENCES

1. F. J. García De Abajo, “Optical excitations in electron microscopy,” Rev. Mod. Phys. **82**, 209 (2010).
2. A. Polman, M. Kociak, and F. J. García de Abajo, “Electron-beam spectroscopy for nanophotonics,” Nat. Mater. **18**, 1158–1171 (2019).
3. F. J. García De Abajo and V. Di Giulio, “Optical excitations with electron beams: challenges and opportunities,” ACS Photon. **8**, 945–974 (2021).
4. L. J. Wong, I. Kaminer, O. Ilic, J. D. Joannopoulos, and M. Soljačić, “Towards graphene plasmon-based free-electron infrared to X-ray sources,” Nat. Photonics **10**, 46–52 (2016).
5. M. Shentcis, A. K. Budniak, X. Shi, R. Dahan, Y. Kurman, M. Kalina, H. Herzig Sheinfux, M. Blei, M. K. Svendsen, Y. Amouyal, S. Tongay, K. S. Thygesen, F. H. L. Koppens, E. Lifshitz, F. J. García de Abajo, L. J. Wong, and I. Kaminer, “Tunable free-electron X-ray radiation from van der Waals materials,” Nat. Photonics **14**, 686–692 (2020).
6. P. A. Cherenkov, “Radiation from high-speed particles,” Science **131**, 136–142 (1960).
7. I. E. Tamm, “General characteristics of Vavilov-Cherenkov radiation,” Science **131**, 206–210 (1960).
8. I. M. Frank, “Optics of light sources moving in refractive media,” Science **131**, 702–712 (1960).
9. V. L. Ginzburg, “Transition radiation and transition scattering,” Phys. Scr. **1982**, 182 (1982).
10. I. Frank and I. Tamm, “Radiation by uniformly moving sources (Vavilov–Cherenkov effect, transition radiation, and other phenomena),” Physics-Uspekhi **39**, 973–982 (1996).
11. S. J. Smith and E. M. Purcell, “Visible light from localized surface charges moving across a grating,” Phys. Rev. **92**, 1069 (1953).
12. Z. Su, B. Xiong, Y. Xu, Z. Cai, J. Yin, R. Peng, and Y. Liu, “Manipulating Cherenkov radiation and Smith–Purcell radiation by artificial structures,” Adv. Opt. Mater. **7**, 1801666 (2019).
13. P. Cherenkov, “Visible glow of pure liquids under the action of γ-radiation,” Dokl. Akad. Nauk SSSR **2**, 451 (1934).
14. P. A. Cherenkov, “Visible radiation produced by electrons moving in a medium with velocities exceeding that of light,” Phys. Rev. **52**, 378–379 (1937).
15. I. E. Tamm and I. M. Frank, “Coherent visible radiation of fast electrons passing through matter,” Dokl. Akad. Nauk SSSR **14**, 107–112 (1937).
16. M. Günay, Y. L. Chuang, and M. E. Tasgin, “Continuously-tunable Cherenkov-radiation-based detectors via plasmon index control,” Nanophotonics **9**, 1479–1489 (2020).
17. X. Lin, H. Hu, S. Easo, Y. Yang, Y. Shen, K. Yin, M. P. Blago, I. Kaminer, B. Zhang, H. Chen, J. Joannopoulos, M. Soljačić, and Y. Luo, “A Brewster route to Cherenkov detectors,” Nat. Commun. **12**, 5554 (2021).
18. Y. Gong, Q. Zhou, M. Hu, Y. Zhang, X. Li, H. Gong, J. Wang, D. Liu, Y. Liu, Z. Duan, and J. Feng, “Some advances in theory and experiment of high-frequency vacuum electron devices in China,” IEEE Trans. Plasma Sci. **47**, 1971–1990 (2019).
19. T. M. Shaffer, E. C. Pratt, and J. Grimm, “Utilizing the power of Cerenkov light with nanotechnology,” Nat. Nanotechnol. **12**, 106–117 (2017).
20. S. Liu, P. Zhang, W. Liu, S. Gong, R. Zhong, Y. Zhang, and M. Hu, “Surface polariton Cherenkov light radiation source,” Phys. Rev. Lett. **109**, 153902 (2012).
21. M. Silveirinha, “A low-energy Cherenkov glow,” Nat. Photonics **11**, 269–271 (2017).
22. F. Liu, L. Xiao, Y. Ye, M. Wang, K. Cui, X. Feng, W. Zhang, and Y. Huang, “Integrated Cherenkov radiation emitter eliminating the electron velocity threshold,” Nat. Photonics **11**, 289–292 (2017).
23. P. Shekhar, S. Pendharker, H. Sahasrabudhe, D. Vick, M. Malac, R. Rahman, and Z. Jacob, “Extreme ultraviolet plasmonics and Cherenkov radiation in silicon,” Optica **5**, 1590–1596 (2018).
24. A. A. Govyadinov, A. Konečná, A. Chuvilin, S. Vélez, I. Dolado, A. Y. Nikitin, S. Lopatin, F. Casanova, L. E. Hueso, J. Aizpurua, and R. Hillenbrand, “Probing low-energy hyperbolic polaritons in van der Waals crystals with an electron microscope,” Nat. Commun. **8**, 95 (2017).
25. T. Qu, F. Liu, Y. Lin, K. Cui, X. Feng, W. Zhang, and Y. Huang, “Cherenkov radiation generated in hexagonal boron nitride using extremely low-energy electrons,” Nanophotonics **9**, 1491–1499 (2020).
26. C. Maciel-Escudero, A. Konečná, R. Hillenbrand, and J. Aizpurua, “Probing and steering bulk and surface phonon polaritons in uniaxial materials using fast electrons: hexagonal boron nitride,” Phys. Rev. B **102**, 115431 (2020).
27. C. Luo, M. Ibanescu, S. G. Johnson, and J. D. Joannopoulos, “Cerenkov radiation in photonic crystals,” Science **299**, 368–371 (2003).
28. S. Xi, H. Chen, T. Jiang, L. Ran, J. Huangfu, B. I. Wu, J. A. Kong, and M. Chen, “Experimental verification of reversed Cherenkov radiation in left-handed metamaterial,” Phys. Rev. Lett. **103**, 194801 (2009).
29. Z. Duan, X. Tang, Z. Wang, Y. Zhang, X. Chen, M. Chen, and Y. Gong, “Observation of the reversed Cherenkov radiation,” Nat. Commun. **8**, 14901 (2017).
30. S. Gong, M. Hu, Z. Wu, H. Pan, H. Wang, K. Zhang, R. Zhong, J. Zhou, T. Zhao, D. Liu, W. Wang, C. Zhang, and S. Liu, “Direction controllable inverse transition radiation from the spatial dispersion in a graphene-dielectric stack,” Photon. Res. **7**, 1154–1160 (2019).
31. X. Zhang, M. Hu, Z. Zhang, Y. Wang, T. Zhang, X. Xu, T. Zhao, Z. Wu, R. Zhong, D. Liu, Y. Wei, Y. Gong, and S. Liu, “High-efficiency threshold-less Cherenkov radiation generation by a graphene hyperbolic grating in the terahertz band,” Carbon **183**, 225–231 (2021).
32. L. Lu, J. D. Joannopoulos, and M. Soljačić, “Topological photonics,” Nat. Photonics **8**, 821–829 (2014).
33. T. Ozawa, H. M. Price, A. Amo, N. Goldman, M. Hafezi, L. Lu, M. C. Rechtsman, D. Schuster, J. Simon, O. Zilberberg, and I. Carusotto, “Topological photonics,” Rev. Mod. Phys. **91**, 015006 (2019).
34. H. N. S. Krishnamoorthy, Z. Jacob, E. Narimanov, I. Kretzschmar, and V. M. Menon, “Topological transitions in metamaterials,” Science **336**, 205–209 (2012).

35. R. Yu, R. Alaee, R. W. Boyd, and F. J. G. De Abajo, "Ultrafast topological engineering in metamaterials," Phys. Rev. Lett. **125**, 037403 (2020).
36. A. J. Sternbach, S. H. Chae, S. Latini, A. A. Rikhter, Y. Shao, B. Li, D. Rhodes, B. Kim, P. J. Schuck, X. Xu, X.-Y. Zhu, R. D. Averitt, J. Hone, M. M. Fogler, A. Rubio, and D. N. Basov, "Programmable hyperbolic polaritons in van der Waals semiconductors," Science **371**, 617–620 (2021).
37. A. N. Grigorenko, M. Polini, and K. S. Novoselov, "Graphene plasmonics," Nat. Photonics **6**, 749–758 (2012).
38. G. X. Ni, A. S. McLeod, Z. Sun, L. Wang, L. Xiong, K. W. Post, S. S. Sunku, B. Y. Jiang, J. Hone, C. R. Dean, M. M. Fogler, and D. N. Basov, "Fundamental limits to graphene plasmonics," Nature **557**, 530–533 (2018).
39. F. H. L. Koppens, D. E. Chang, and F. J. García De Abajo, "Graphene plasmonics: a platform for strong light–matter interactions," Nano Lett. **11**, 3370–3377 (2011).
40. A. Poddubny, I. Iorsh, P. Belov, and Y. Kivshar, "Hyperbolic metamaterials," Nat. Photonics **7**, 948–957 (2013).
41. Y. C. Chang, C. H. Liu, C. H. Liu, S. Zhang, S. R. Marder, E. E. Narimanov, Z. Zhong, and T. B. Norris, "Realization of mid-infrared graphene hyperbolic metamaterials," Nat. Commun. **7**, 10568 (2016).
42. H. Lin, B. C. P. Sturmberg, K. Te Lin, Y. Yang, X. Zheng, T. K. Chong, C. M. de Sterke, and B. Jia, "A 90-nm-thick graphene metamaterial for strong and extremely broadband absorption of unpolarized light," Nat. Photonics **13**, 270–276 (2019).
43. J. Benedicto, R. Pollès, C. Ciracì, E. Centeno, D. R. Smith, and A. Moreau, "Numerical tool to take nonlocal effects into account in metallo-dielectric multilayers," J. Opt. Soc. Am. A **32**, 1581–1588 (2015).
44. H. Hu, X. Lin, J. Zhang, D. Liu, P. Genevet, B. Zhang, and Y. Luo, "Nonlocality induced Cherenkov threshold," Laser Photon. Rev. **14**, 2000149 (2020).
45. R. Yu, Q. Guo, F. Xia, and F. J. G. de Abajo, "Photothermal engineering of graphene plasmons," Phys. Rev. Lett. **121**, 057404 (2018).
46. H. Hu, D. Gao, X. Lin, S. Hou, B. Zhang, Q. J. Wang, and Y. Luo, "Directing Cherenkov photons with spatial nonlocality," Nanophotonics **9**, 3435–3442 (2020).
47. E. Galiffi, P. A. Huidobro, P. A. D. Gonçalves, N. A. Mortensen, and J. B. Pendry, "Probing graphene's nonlocality with singular metasurfaces," Nanophotonics **9**, 309–316 (2020).
48. S. Raza, S. I. Bozhevolnyi, M. Wubs, and N. A. Mortensen, "Nonlocal optical response in metallic nanostructures," J. Phys. Condens. Matter **27**, 183204 (2015).
49. D. C. Elias, R. V. Gorbachev, A. S. Mayorov, S. V. Morozov, A. A. Zhukov, P. Blake, L. A. Ponomarenko, I. V. Grigorieva, K. S. Novoselov, F. Guinea, and A. K. Geim, "Dirac cones reshaped by interaction effects in suspended grapheme," Nat. Phys. **7**, 701–704 (2011).
50. C. Hwang, D. A. Siegel, S. K. Mo, W. Regan, A. Ismach, Y. Zhang, A. Zettl, and A. Lanzara, "Fermi velocity engineering in graphene by substrate modification," Sci. Rep. **2**, 590 (2012).
51. D. A. Siegel, W. Regan, A. V. Fedorov, A. Zettl, and A. Lanzara, "Charge-carrier screening in single-layer grapheme," Phys. Rev. Lett. **110**, 146802 (2013).
52. T. Stauber, P. Parida, M. Trushin, M. V. Ulybyshev, D. L. Boyda, and J. Schliemann, "Fermi velocity renormalization and optical response," Phys. Rev. Lett. **118**, 266801 (2017).
53. O. Vafek and J. Kang, "Hidden symmetry in twisted bilayer graphene with Coulomb interactions," Phys. Rev. Lett. **125**, 257602 (2020).
54. C. H. Park, F. Giustino, M. L. Cohen, and S. G. Louie, "Velocity renormalization and carrier lifetime in graphene from the electron-phonon interaction," Phys. Rev. Lett. **99**, 086804 (2007).
55. F. Escudero and J. S. Ardenghi, "Fermi velocity reduction in graphene due to enhanced vacuum fluctuations," J. Phys. Condens. Matter **33**, 485502 (2021).
56. J. Duan, G. Álvarez-Pérez, K. V. Voronin, I. Prieto, J. Taboada-Gutiérrez, V. S. Volkov, J. Martín-Sánchez, A. Y. Nikitin, and P. Alonso-González, "Enabling propagation of anisotropic polaritons along forbidden directions via a topological transition," Sci. Adv. **7**, eabf2690 (2021).
57. W. Wu, W. Wu, S. Chen, W. Xu, Z. Liu, R. Lou, L. Shen, H. Luo, H. Luo, S. Wen, X. Yin, X. Yin, and X. Yin, "Weak-value amplification for the optical signature of topological phase transitions," Photon. Res. **8**, B47–B54 (2020).
58. Y. Gelkop, F. Di Mei, S. Frishman, Y. Garcia, L. Falsi, G. Perepelitsa, C. Conti, E. DelRe, and A. J. Agranat, "Hyperbolic optics and superlensing in room-temperature KTN from self-induced k-space topological transitions," Nat. Commun. **12**, 7241 (2021).
59. P. N. Dyachenko, S. Molesky, A. Y. Petrov, M. Störmer, T. Krekeler, S. Lang, M. Ritter, Z. Jacob, and M. Eich, "Controlling thermal emission with refractory epsilon-near-zero metamaterials via topological transitions," Nat. Commun. **7**, 11809 (2016).
60. R. Deshmukh, S. A. Biehs, E. Khwaja, T. Galfsky, G. S. Agarwal, and V. M. Menon, "Long-range resonant energy transfer using optical topological transitions in metamaterials," ACS Photonics **5**, 2737–2741 (2018).
61. Y. Xiang, X. Dai, J. Guo, H. Zhang, S. Wen, and D. Tang, "Critical coupling with graphene-based hyperbolic metamaterials," Sci. Rep. **4**, 5483 (2014).
62. T. T. Lv, Y. X. Li, H. F. Ma, Z. Zhu, Z. P. Li, C. Y. Guan, J. H. Shi, H. Zhang, and T. J. Cui, "Hybrid metamaterial switching for manipulating chirality based on VO_2 phase transition," Sci. Rep. **6**, 23186 (2016).
63. J. Shi, Z. Li, D. K. Sang, Y. Xiang, J. Li, S. Zhang, and H. Zhang, "THz photonics in two dimensional materials and metamaterials: properties, devices and prospects," J. Mater. Chem. C **6**, 1291–1306 (2018).
64. D. N. Basov, M. M. Fogler, and F. J. García De Abajo, "Polaritons in van der Waals materials," Science **354**, aag1992 (2016).